

The double-peaked type I X-ray bursts with different mass accretion rate and fuel composition

Liyu Song,¹ Helei Liu,^{1*} Chunhua Zhu,¹ Guoqing Zhen,¹ Guoliang Lü² and Renxin Xu^{3,4}

¹*School of Physical Science and Technology, Xinjiang University, Urumqi 830046, China*

²*Xinjiang Astronomical Observatory, Chinese Academy of Science, 150 Science 1-Street, Urumqi 830011, China*

³*Department of Astronomy, Peking University, Beijing 100871, China*

⁴*Kavli Institute for Astronomy and Astrophysics, Peking University, Beijing 100871, China*

Accepted XXX. Received YYY; in original form ZZZ

ABSTRACT

Using the MESA code, we have carried out a detailed survey of the available parameter space for the double-peaked type I X-ray bursts. We find that the double-peaked structure appears at mass accretion rate \dot{M} in the range of $\sim (4 - 8) \times 10^{-10} M_{\odot}/\text{yr}$ when metallicity $Z = 0.01$, while in the range of $\sim (4 - 8) \times 10^{-9} M_{\odot}/\text{yr}$ when $Z = 0.05$. Calculations of the metallicity impact suggest that the double peaks will disappear when $Z \lesssim 0.005$ for $\dot{M} = 5 \times 10^{-10} M_{\odot}/\text{yr}$ and $Z \lesssim 0.04$ for $\dot{M} = 5 \times 10^{-9} M_{\odot}/\text{yr}$. Besides, the impacts of base heating Q_b , as well as nuclear reaction waiting points: ^{22}Mg , ^{26}Si , ^{30}S , ^{34}Ar , ^{56}Ni , ^{60}Zn , ^{64}Ge , ^{68}Se , ^{72}Kr have been explored. The luminosity of the two peaks decreases as Q_b increases. $^{68}\text{Se}(p, \gamma)^{69}\text{Br}$ is the most sensitive reaction, the double peaks disappear assuming that $^{56}\text{Ni}(p, \gamma)^{57}\text{Cu}$ and $^{64}\text{Ge}(p, \gamma)^{65}\text{As}$ reaction rates have been underestimated by a factor of 100 and the $^{22}\text{Mg}(\alpha, p)^{25}\text{Al}$ reaction rate has been overestimated by a factor of 100, which indicates that ^{22}Mg , ^{56}Ni , ^{64}Ge , ^{68}Se are possibly the most important nuclear waiting points impedance in the thermonuclear reaction flow to explain the double-peaked bursts. Comparisons to the double-peaked bursts from 4U 1636-53 and 4U 1730-22 suggest that the nuclear origins of double-peaked type I X-ray bursts are difficult to explain the observed larger peak times ($t_{p,1} \gtrsim 4\text{ s}$, $t_{p,2} \gtrsim 8\text{ s}$) and smaller peak ratio ($r_{1,2} \lesssim 0.5$). The composition of ashes from double-peaked bursts is very different from the single-peaked bursts especially for the heavier p-nuclei.

Key words: stars:neutron star – X-rays: burst – double-peak

1 INTRODUCTION

In low-mass X-ray binaries (LMXBs), the unstable burning of accreted fuel on the surface of a neutron star (NS) triggers type I X-ray bursts (Lewin et al. 1993; Strohmayer & Bildsten 2006; Galloway et al. 2008). The typical type I X-ray burst exhibits a rapid rise (1–5 s) and an exponential decay within 10–100 s, showing a single peak in the light curve profile. However, some observed double-peaked bursts have been found in several NS-LMXBs (Penninx et al. 1989; Bhattacharyya & Strohmayer 2006; Li et al. 2021), and the origins of the double peaks feature can be categorized into two types: the instrumental origin caused by a photospheric radius expansion (PRE) and the astrophysical origin (Bult et al. 2019). For the former, the temperature of the photosphere temporarily shifts out of the instrument passband due to radius expansion (Paczynski 1983), which causes the dip in the observed X-ray rate, while the bolometric luminosity shows a single peak. For the latter, the double-peaked structure exists in the bolometric luminosity.

Non-PRE bursts with double-peaked structure have been detected in five bursters, e.g., 4U 1636-536 (Bhattacharyya & Strohmayer 2006; Li et al. 2021), 4U 1608-52 (Penninx et al. 1989; Güver et al. 2021), GX 17+2 (Kuulkers et al. 2002), GRS 1741.9-

2853 (Pike et al. 2021) and 4U 1730-22 (Bult et al. 2022; Chen et al. 2023), although PRE bursts with double peak structures both in X-rays and bolometric luminosity have been observed from 4U 1608-52 (Jaisawal et al. 2019) and SAX J1808.4-3658 (Bult et al. 2019).

Several theories have been proposed to explain the double-peaked bursts: e.g., the heat transport impedance from the other zone caused a dip in the light curve in a two-zone accreting model (Regev & Livio 1984), the two steps generation/release of the thermonuclear energy (Sztajno et al. 1985; Fujimoto et al. 1988), scattering from an accretion-disk corona (Melia 1987; Melia & Zylstra 1992), thermonuclear flame spreading model (e.g., ignition at high latitude but stalls on the equator) (Bhattacharyya & Strohmayer 2006). However, it was argued that the two-zone model is too coarse, the double peaks structure will disappear with increasing the zones (Fisker et al. 2004); the recurrence times from the two steps release of the thermonuclear energy model are two orders of magnitude larger than observations (Sztajno et al. 1985); the observed multi-peaked X-ray burst from 4U 1636-53 against burst induced accretion-disk corona model (Penninx et al. 1987); the flame spreading model has drawbacks that triple-peaked and quadruple-peaked bursts cannot be explained (Zhang et al. 2009; Li et al. 2021). Moreover, these models cannot reproduce the light curve of the observed double-peaked bursts (Bhattacharyya & Strohmayer 2006; Li et al. 2021).

Asyali & Joss (1982) proposed a double-peaked structure using

* E-mail: heleiliu@xju.edu.cn

the stellar evolution code ASTRA, the first very sharp peak results from the helium burning, and the second peak results from the energy generation of mixed hydrogen/helium flashes via the rp process. Such a double-peaked profile was also noticed by Hanawa & Fujimoto (1984). Both works adopted the approximation network, Ayasli & Joss (1982) assumed a 15 s characteristic timescale to synthesize nickel from sulfur, which leads to a broad peak separation time. Hanawa & Fujimoto (1984) adopted 2.327 s instead of 15 s, which results in a very short peak separation time as 1.8 s. Both failed to explain 4–7 s peak separation of the double-peaked burst observations (Li et al. 2021).

Fisker et al. (2004) suggested a nuclear waiting point impedance in the thermonuclear reaction flow to explain the double peak structure using the modified version of AGILE (Liebendörfer et al. 2002). However, only the nuclear reaction waiting points: ^{22}Mg , ^{26}Si , ^{30}S , ^{34}Ar are considered, the impact of the rp process potential waiting points: ^{56}Ni , ^{60}Zn , ^{64}Ge , ^{68}Se , ^{72}Kr on the double peak structure have not been explored (Schatz & Rehm 2006). Lampe et al. (2016) simulated the nuclear origins of double-peaked bursts using the KEPLER code, and they found that the double-peak structures are prominent in the higher metallicity ($Z = 0.1$) and low accretion rates models. However, a larger than typical metallicity ($Z = 0.01$) is required to produce the double-peaked light curves, which conflicts with the models in Ayasli & Joss (1982), where the double-peaked burst is produced with $Z = 0.01$. Recently, Bult et al. (2019) interpreted that the bright double-peaked bursts are due to the local Eddington limits associated with the H and He layers of the NS envelope.

Understanding the above mechanisms is important because the light curves and temperature profiles of the double-peaked bursts, as well as triple-peaked/quadruple-peaked bursts, have not yet been successfully explained. A detailed survey of the available parameter space such as mass accretion rate and metallicity is important to understand the nuclear origins of the double-peaked bursts. Besides, the base luminosity which depends on Q_b and \dot{M} , has a significant impact on the typically single-peaked type I X-ray burst (Meisel 2018; Dohi et al. 2021; Zhen et al. 2023) and the frequency of the mHz quasi-period oscillations (Keek et al. 2014; Liu et al. 2023). As a result, the investigation of the impact of Q_b on the double-peaked structure is one of our purposes in this work.

In this study, we simulate the nuclear origins of the double-peaked type I X-ray bursts using the MESA (Modules for Experiments in Stellar Astrophysics) code (Paxton et al. 2011, 2013, 2015, 2018). We describe the details of the input physics, reaction network, and fuel composition in Section 2. In Section 3, we present our simulations of double-peaked bursts with high and ordinary metallicity, respectively. The impacts of mass accretion rate, metallicity, base heating, and more nuclear reaction waiting points on the double-peaked structure are discussed, and the parameter space for the conditions of double-peaked bursts is found. In Section 4, we compare our results with the observations from 4U 1636-53 and 4U 1730-22. The composition of ashes from double-peaked bursts is also explored. We summarize our conclusions in Section 5.

2 MODEL

We utilize the one-dimensional stellar evolution code MESA version 9793 to simulate double-peaked bursts under different conditions. The details of the numerical approach and physics models can be found in the associated instrumentation papers (Paxton et al. 2011, 2013, 2015, 2018). Here, we summarize the most relevant details for

this work. The envelope is 0.01 km thick, with an inner boundary of NS mass $M = 1.4 M_\odot$ and radius $R = 11.2$ km, which is the same as (Meisel 2018). We adopt base heat $Q_b = 0.1, 0.2, 0.3, 0.4$ MeV/u to consider the heat flow from the crust into the envelope, which is consistent with the constraint of $Q_b < 0.5$ MeV/u (Meisel 2018) and $Q_b \approx 0.3 - 0.4$ MeV/u calculated by Dohi et al. (2021). In MESA, this is achieved by fixing the luminosity at the base of the envelope, the base luminosity can be written as $L_{\text{base}} = \dot{M}Q_b$. The mass accretion rate is adopted the values close to $4.75 \times 10^{-10} M_\odot/\text{yr}$ and $(0.2 - 1) \times 10^{-8} M_\odot/\text{yr}$ that are responsible for the double-peaked bursts in the previous works, the former is based on Ayasli & Joss (1982) and the latter is based on Lampe et al. (2016). The composition of the accreted fuel is determined by assuming the helium fraction (Y) changes with metallicity according to $Y = 0.24 + 1.75Z$ (Lampe et al. 2016), then the fraction of hydrogen (X) can be inferred by $X = 1 - Y - Z$.

The envelope is discretized into ~ 1000 zones, and the local gravity in a zone is corrected for general relativity (GR) effects using a post-Newtonian correction, which is achieved by setting “*use_GR_factors = .true.*” (Paxton et al. 2011, 2015). Adaptive time and spatial resolution were employed by setting “*varcontrol_target = 1d-3*” and “*mesh_delt_coeff = 1.0*” (Meisel 2018).

We adopted the *rp.net* nuclear reaction network, which includes 304 isotopes (Fisker et al. 2007), and the nuclear reaction rates from the REACLIB V2.2 library (Cyburt et al. 2010).

The nuclear waiting point impedance is explored by variation of the $^{22}\text{Mg}(\alpha, p)^{25}\text{Al}$, $^{26}\text{Si}(\alpha, p)^{29}\text{P}$, $^{30}\text{S}(\alpha, p)^{33}\text{Cl}$, $^{34}\text{Ar}(\alpha, p)^{37}\text{K}$, $^{56}\text{Ni}(p, \gamma)^{57}\text{Cu}$, $^{60}\text{Zn}(p, \gamma)^{61}\text{Ga}$, $^{64}\text{Ge}(p, \gamma)^{65}\text{As}$, $^{68}\text{Se}(p, \gamma)^{69}\text{Br}$, $^{72}\text{Kr}(p, \gamma)^{73}\text{Rb}$ reaction up and down via a factor 100 (Fisker et al. 2004; Cyburt et al. 2016), where the factor roughly means the reactions had been underestimated (up) or overestimated (down) by a factor of 100 for the reaction rate uncertainty (Hu et al. 2021).

A series of double-peaked bursts were simulated with models differed in mass accretion rate (\dot{M}), composition (X, Y, Z), base heat (Q_b) and the nuclear reaction waiting points.

3 RESULTS

Using MESA, we have carried out a series of numerical calculations to study the properties of double-peaked bursts. Our method and the physics inputs that we employed are described in the preceding section. The two different nuclear origins of double-peaked type I X-ray bursts are obtained (standard model 1 and standard model 2). The effects of mass accretion rate, metallicity, base heating, as well as the nuclear reaction waiting points on the properties of double-peaked structure are examined.

3.1 The nuclear origins of double-peaked type I X-ray bursts

Ayasli & Joss (1982) studied the thermonuclear flashes on accreting neutron stars using a modified version of the stellar evolution code ASTRA, an approximation network including twenty nuclear species was used. The double-peaked structure was found with parameters: $\dot{M} = 4.75 \times 10^{-10} M_\odot/\text{yr}$, fuel composition $X = 0.69$, $Y = 0.30$ and $Z = 0.01$. The explanation corresponding to the double peaks is as follows: the first peak results from helium burning, the depletion of helium causes the dip in the luminosity, and the subsequent consumption of hydrogen via the rp process leads to the second peak. Lampe et al. (2016) simulated thermonuclear X-ray bursts by use of the KEPLER code, they found that the double-peaked structures are prominent in the higher metallicity models ($Z = 0.1$) at low mass

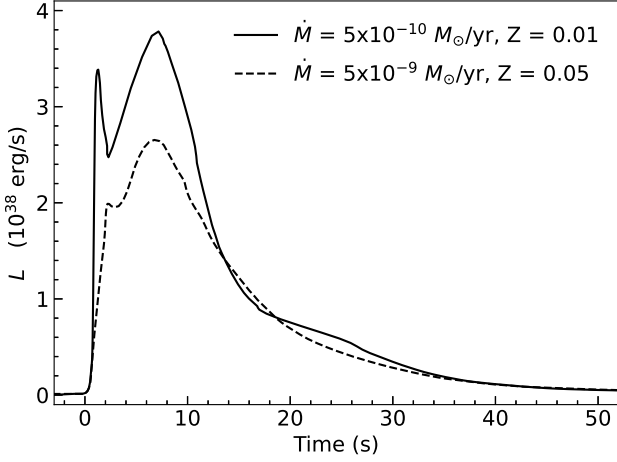


Figure 1. Double-peaked bursts with low mass accretion rate ($\dot{M} = 5 \times 10^{-10} M_{\odot}/\text{yr}$) at metallicity $Z = 0.01$ (solid line) and an order of magnitude higher mass accretion rate $\dot{M} = 5 \times 10^{-9} M_{\odot}/\text{yr}$ at $Z = 0.05$ (dashed line). For convenience, the former is called standard model 1, the latter is called standard model 2. In both models, the value of base heating is set as $Q_b = 0.1 \text{ MeV/u}$.

accretion rates ($\dot{M} = 3.5 \times 10^{-9} M_{\odot}/\text{yr}$), as mass accretion rate increases, the two peaks become indistinguishable. Their explanation is as follows: the first peak is a helium flash, which convects rapidly to the surface in less than a second, and the second peak occurs due to a nuclear waiting point impedance.

Both the accretion rate and metallicity in [Ayasli & Joss \(1982\)](#) (for convenience, we call it case 1) are one order of magnitude lower than that in [Lampe et al. \(2016\)](#) (case 2). So far, only a little attention has been paid to studying the conditions for double-peaked bursts. Here, we explore it with the use of MESA. By sequences of simulations with different mass accretion rates and metallicity, we obtained the double-peaked bursts corresponding to the above two scenarios. The results are shown in Fig. 1. The presence of double-peaked structure in our models with low mass accretion rate ($\dot{M} = 5 \times 10^{-10} M_{\odot}/\text{yr}$) at ordinary metallicity ($Z = 0.01$) and an order of magnitude higher mass accretion rate ($\dot{M} = 5 \times 10^{-9} M_{\odot}/\text{yr}$) at $Z = 0.05$ indicates that the nuclear origins of the double-peaked bursts can be simulated consistently with MESA. The rest physics inputs are the same between the two models, e.g., $M = 1.4 M_{\odot}$, $R = 11.2 \text{ km}$, $Q_b = 0.1 \text{ MeV/u}$, which can be found in Table 1 from the Appendix. These two models are marked as our standard models in two cases. We can find that the peak luminosity and peak ratio are different in the two cases. The dips between the two peaks are more obvious with lower mass accretion rate and metallicity (standard model 1). From the perspective of observations, the rise time of the first and second peaks, the separation time between the two peaks, as well as the peak flux ratio are varied among the samples of double-peaked bursts ([Li et al. 2021](#)). It's worth investigating whether double-peaked bursts can have a nuclear origin influenced by different factors, such as mass accretion rate, metallicity, base heating, and nuclear reaction waiting points. These factors will be explored in the following.

3.2 Impact of mass accretion rate

Mass accretion rate plays an important role in type I X-ray burst ([Fujimoto et al. 1981](#); [Galloway & Keek 2021](#)). At high mass accretion rate ($\dot{M} \gtrsim 10^{-8} M_{\odot}/\text{yr}$), the accreted fuel burns sta-

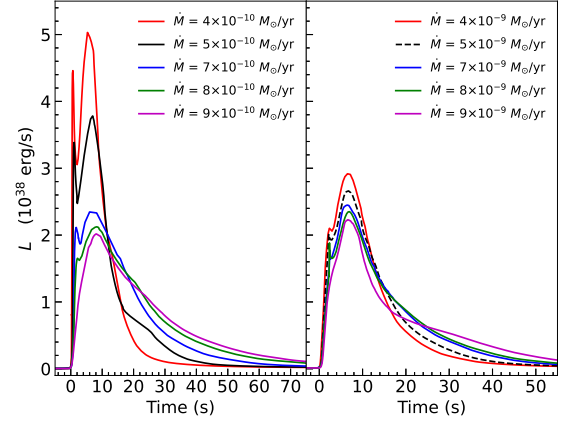


Figure 2. Double-peaked bursts for the standard model and additional models with the same parameter values as those of the standard model except for the mass accretion rate. Left: Light curves as functions of mass accretion rate based on standard model 1. Right: Light curves as a function of mass accretion rate based on standard model 2. In both cases, the double-peaked structures are prominent in the low mass accretion rate and will disappear as the mass accretion rate increases.

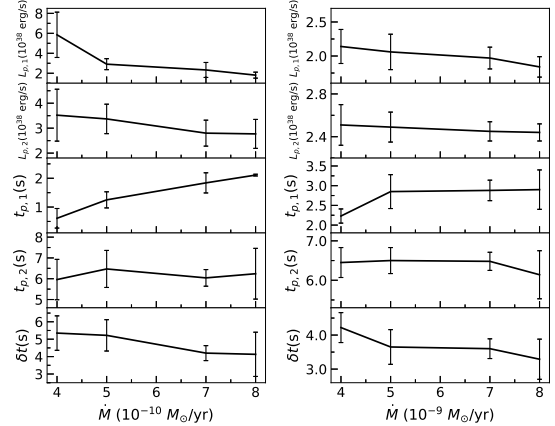


Figure 3. The averaged values with 1σ errorbars of the first and second peak luminosity ($L_{p,1}$, $L_{p,2}$), the rise time of the first and second peak ($t_{p,1}$, $t_{p,2}$), and peak interval time δt as a function of \dot{M} . Left: models 3-6 in case 1 (corresponding to the left panel of Fig. 2). Right: models 7-10 in case 2 (corresponding to the right panel of Fig. 2).

bly. At relatively high mass accretion rate ($10^{-9} M_{\odot}/\text{yr} \lesssim \dot{M} \lesssim 10^{-8} M_{\odot}/\text{yr}$), the mixed H/He burst occurs with a long tail from rp process. At low mass accretion rate ($10^{-10} M_{\odot}/\text{yr} \lesssim \dot{M} \lesssim 10^{-9} M_{\odot}/\text{yr}$), pure helium X-ray burst occurs. At still lower mass accretion rate ($\dot{M} \lesssim 10^{-10} M_{\odot}/\text{yr}$), as the unstable hydrogen burning occurs before the unstable helium burning, the mixed H/He burst occurs. There have been many efforts to explore the effects of mass accretion rate on thermonuclear bursts ([Ayasli & Joss 1982](#); [Lampe et al. 2016](#); [Meisel 2018](#); [Johnston et al. 2020](#)), which leads us to understand more clearly about the \dot{M} dependent type I X-ray burst. However, the parameter space of \dot{M} for double-peaked bursts is unclear. We varied the mass accretion rate based on standard models 1 and 2. The results are illustrated in Fig. 2.

We have plotted the 11th burst for each simulation in Fig. 2 to

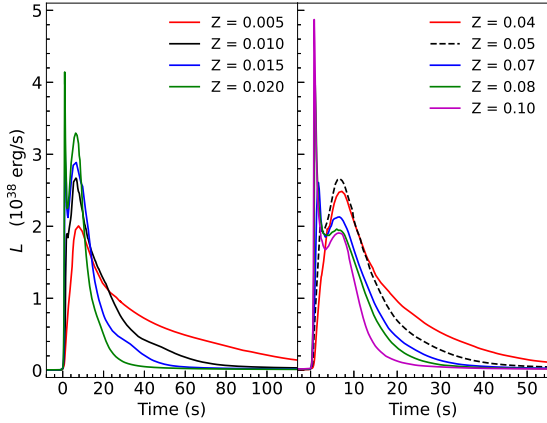


Figure 4. Same as Fig. 2 for the standard model and additional models with the same parameter values as those of the standard model except for the fuel composition due to the change of metallicity. Left: Light curves as a function of metallicity based on model 5. Right: Light curves as a function of metallicity based on standard model 2. In both cases, the double-peaked structures are prominent in the relatively higher metallicity and will disappear as metallicity decreases.

ensure a consistent ashes layer following Lampe et al. (2016). The double-peaked structures are prominent in the lower mass accretion rate models, while the helium peak is suppressed at higher mass accretion rate in the two cases, which is consistent with Lampe et al. (2016). In case 1 (left panel of Fig. 2), the double-peaked structure appears at mass accretion rate in the range of $\sim (4-8) \times 10^{-10} M_{\odot}/\text{yr}$ for $Z = 0.01$. The double-peaked structure disappears at $\dot{M} = 9 \times 10^{-10} M_{\odot}/\text{yr}$ for $Z = 0.01$. In case 2 (right panel of Fig. 2), the double-peaked structure appears at mass accretion rate in the range of $\sim (4-8) \times 10^{-9} M_{\odot}/\text{yr}$ for $Z = 0.05$. The double-peaked structure disappears at $\dot{M} = 9 \times 10^{-9} M_{\odot}/\text{yr}$ for $Z = 0.05$.

The results for the parameter variation with mass accretion rate are shown in Fig. 3. With increase of \dot{M} , both the first and second peak luminosities ($L_{p,1}$, $L_{p,2}$) decrease, the first peak time ($t_{p,1}$) increases, the second peak time ($t_{p,2}$) is almost constant, the peak separation time δt decreases. This is because at a low mass accretion rate, the first peak is a helium flash with a very short rise time, with the increase of the mass accretion rate, the amount of pure helium layer at the base of the accreted material decreases, and mixed H/He burst occurs, as a result, the rise time of the first peak increases, the peak separation time decreases and the peak luminosity decreases. The changes in the two cases are almost consistent. The values of $L_{p,1}$, $L_{p,2}$, $t_{p,1}$, $t_{p,2}$, and δt can be found in Table 2 from the Appendix. Besides, the other properties for double-peaked bursts such as burst strength (α), burst energy (E_{burst}), recurrence time (ΔT), as well as the first ($L_{p,1}$) and second ($L_{p,2}$) peak luminosity are also obtained and illustrated in Table 2 from the Appendix. We discard the first two bursts and the last burst of each model to calculate these values with 1σ uncertainty. The number of bursts and bursts with two peaks of each model are shown in Table 1 in the appendix.

3.3 Impact of metallicity

The metallicity of the accreting matter has an important influence on the properties of thermonuclear bursts. We present the results for several models wherein the initial metallicity of accreting matter is varied in their standard values. The results are shown in Fig. 4.

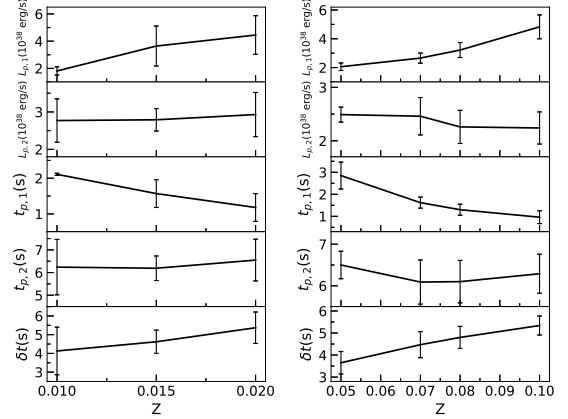


Figure 5. Same as Fig. 3 but as a function of Z . Left: models 11-13 in case 1 (corresponding to the left panel of Fig. 4). Right: models 14-17 in case 2 (corresponding to the right panel of Fig. 4).

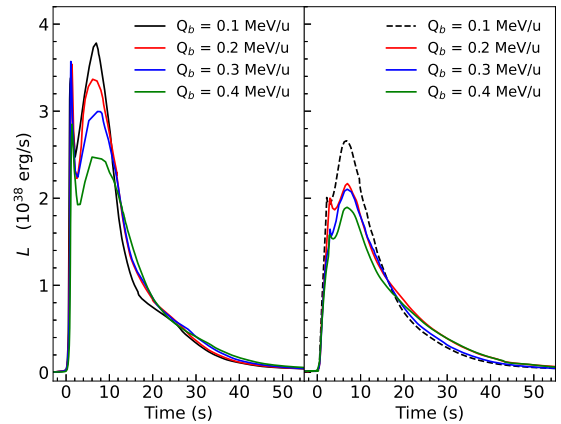


Figure 6. Same as Fig. 2 for the standard model and additional models with the same parameter values as those of the standard model except for the base heating Q_b . Left: Light curves as a function of base heating based on standard model 1. Right: Light curves as a function of base heating based on standard model 2. In both cases, the double-peaked structures will not disappear as Q_b increases.

We find that the double-peaked structures are prominent in the high metallicity models, the first helium peak will be suppressed at lower metallicity in the two cases.

Fig. 5 shows the parameter variation with metallicity. The first peak luminosity $L_{p,1}$ increases as metallicity increases, while the second peak luminosity $L_{p,2}$ changes irregularly as Z increases. The first peak time $t_{p,1}$ decreases as Z increases, and the second peak time $t_{p,2}$ almost remains constant as Z increases, resulting in the peak separation time increases.

As the metallicity catalyzes the burning of hydrogen via the CNO cycle, increased z increases the pure helium layer at the base of the accreted matter. An increased pure helium layer causes the first peak luminosity to increase and the first peak to rise rapidly.

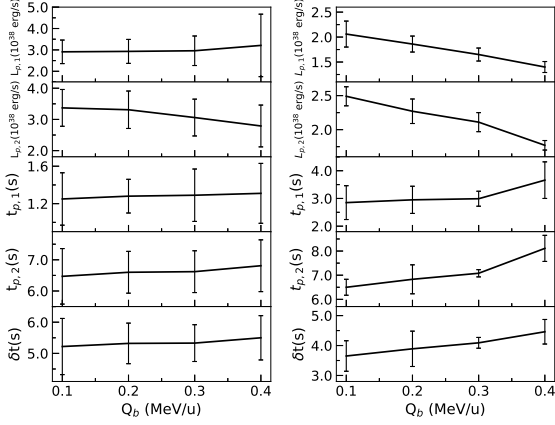


Figure 7. Same as Fig. 3 but as a function of Q_b . Left: models 18-20 in case 1 (corresponding to the left panel of Fig. 6). Right: models 21-23 in case 2 (corresponding to the right panel of Fig. 6).

3.4 Impact of base heating

The base heating is included for type I X-ray burst simulations which consider the NS envelope (Heger et al. 2007; Meisel 2018; Johnston et al. 2020), this additional heating represents the heat flowing from the underlying NS crust to the envelope, and specified by the parameter Q_b . Most models adopt a value of $Q_b = 0.1 - 0.15$ MeV/u (Haensel & Zdunik 1990; Galloway & Keek 2021). Meisel (2018) obtained the constraint of $Q_b < 0.5$ MeV/u from the observations of GS 1826-24, Dohi et al. (2021) calculated the values of $Q_b \approx 0.3 - 0.4$ MeV/u with use of HERES code, which covers the entire NS regions. We explore the effects of Q_b on the properties of double-peaked bursts. The results are presented in Fig. 6. We find that the double-peaked structures are prominent at lower base heating and will not disappear as Q_b increases.

Fig. 7 exhibits the parameter variation with base heating. We can see from the left panel of Fig. 7 that the first peak luminosity $L_{p,1}$, the first and second peak time, as well as the peak separation time, remain nearly constant, the second peak luminosity $L_{p,2}$ decreases as Q_b increases. In the right panel of Fig. 7, we can see that both the first and second peak luminosities decrease as Q_b increases, the first peak rise time $t_{p,1}$, the second peak time $t_{p,2}$ and the peak separation time δt increase as Q_b increases. This is because the hydrogen burning via hot CNO cycle lasts longer with smaller Q_b , as a result, as Q_b increases, the amount of pure helium layer decreases, which leads to the decrease of the peak luminosity and increase of the peak time. Our results indicate that the Q_b effect is more sensitive to the double-peaked bursts in case 2.

3.5 Impact of the nuclear reaction waiting points

Fisker et al. (2004) proposed a nuclear waiting point impedance in the thermonuclear reaction flow to explain the double-peaked burst observations. The uncertainty in the theoretical (α, p) -rates ^{30}S and ^{34}Ar is studied. So far, no experimental data exist for the specific cases of α -capture on ^{22}Mg , ^{26}Si , ^{30}S , ^{34}Ar or proton-capture on ^{56}Ni , ^{60}Zn , ^{64}Ge , ^{68}Se and ^{72}Kr , although Hu et al. (2021) explored the new $^{22}\text{Mg}(\alpha, p)^{25}\text{Al}$ reaction rate without direct experiment measurement and found 6 orders of magnitude lower than the previous theoretical model. We systematically investigate the uncertainty in the theoretical (α, p) -rates ^{22}Mg , ^{26}Si , ^{30}S , ^{34}Ar and (p, γ) -rates

Table 1. The nuclear reaction waiting points impact the double-peaked bursts in the standard model 1.

Rank	Reaction	Type ^a	Sensitivity ^b
1	$^{68}\text{Se}(p, \gamma)^{69}\text{Br}$	U	14.93
2	$^{22}\text{Mg}(\alpha, p)^{25}\text{Al}$	D	14.71
3	$^{60}\text{Zn}(p, \gamma)^{61}\text{Ga}$	U	13.54
4	$^{26}\text{Si}(\alpha, p)^{29}\text{P}$	D	12.71
5	$^{22}\text{Mg}(\alpha, p)^{25}\text{Al}$	U	10.32
6	$^{60}\text{Zn}(p, \gamma)^{61}\text{Ga}$	D	9.09
7	$^{26}\text{Si}(\alpha, p)^{29}\text{P}$	U	8.65
8	$^{34}\text{Ar}(\alpha, p)^{37}\text{K}$	U	7.71
9	$^{30}\text{S}(\alpha, p)^{33}\text{Cl}$	U	6.44
10	$^{68}\text{Se}(p, \gamma)^{69}\text{Br}$	D	5.56
11	$^{30}\text{S}(\alpha, p)^{33}\text{Cl}$	D	5.51
12	$^{56}\text{Ni}(p, \gamma)^{57}\text{Cu}$	U	4.61
13	$^{56}\text{Ni}(p, \gamma)^{57}\text{Cu}$	D	3.10
14	$^{72}\text{Kr}(p, \gamma)^{73}\text{Rb}$	D	2.71
15	$^{64}\text{Ge}(p, \gamma)^{65}\text{As}$	D	2.55
16	$^{64}\text{Ge}(p, \gamma)^{65}\text{As}$	U	2.53
17	$^{72}\text{Kr}(p, \gamma)^{73}\text{Rb}$	U	1.29
18	$^{34}\text{Ar}(\alpha, p)^{37}\text{K}$	D	0.97

^a Up(U) and down(D) represent the reaction rate changes of $\times 100$ and $/100$, respectively.

^b $E_{LC}^{(k)}$ in units of 10^{37} erg.

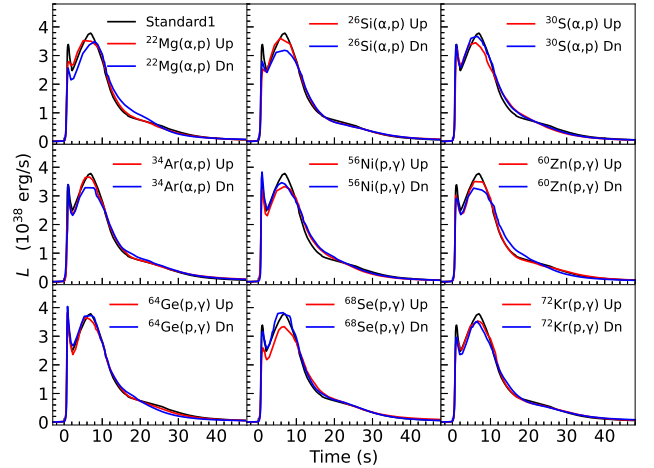


Figure 8. Changes in double-peaked burst light curves induced by variation of the nuclear reaction waiting points up (red) and down (blue), the dotted line represents the standard model 1. Up indicates a rate increase by a factor of 100, and Dn indicates a rate divided by a factor of 100.

^{56}Ni , ^{60}Zn , ^{64}Ge , ^{68}Se , ^{72}Kr on the double-peaked bursts. To explore this effect, we span the reaction rate change of $/100$ (down) to $\times 100$ (up) following Cyburt et al. (2016). Factor 100 was chosen to ensure no sensitivity is missed, and such large uncertainties were found in the theoretical reaction rates via the Hauser-Feshbach approach (Rauscher & Thielemann 2000).

To quantify the influence of the reaction rate variation on double-peaked bursts, we adopt the sensitive value E_{LC}^k defined in Cyburt et al. (2016):

$$E_{LC}^{(k)} = \int |\langle L_k(t) \rangle - \langle L_0(t) \rangle| dt \quad (1)$$

where $L_k(t)$ is the light curve of each variation k , $L_0(t)$ is the luminosity of the standard model.

Table 2. The nuclear reaction waiting points that impact the double-peaked bursts in the standard model 2.

Rank	Reaction	Type ^a	Sensitivity ^b
1	$^{68}\text{Se}(p, \gamma)^{69}\text{Br}$	D	22.47
2	$^{56}\text{Ni}(p, \gamma)^{57}\text{Cu}$	D	11.36
3	$^{30}\text{S}(\alpha, p)^{33}\text{Cl}$	U	9.58
4	$^{22}\text{Mg}(\alpha, p)^{25}\text{Al}$	D	9.21
5	$^{64}\text{Ge}(p, \gamma)^{65}\text{As}$	D	8.71
6	$^{22}\text{Mg}(\alpha, p)^{25}\text{Al}$	U	8.46
7	$^{34}\text{Ar}(\alpha, p)^{37}\text{K}$	U	6.35
8	$^{64}\text{Ge}(p, \gamma)^{65}\text{As}$	U	6.33
9	$^{60}\text{Zn}(p, \gamma)^{61}\text{Ga}$	U	5.14
10	$^{34}\text{Ar}(\alpha, p)^{37}\text{K}$	D	4.73
11	$^{68}\text{Se}(p, \gamma)^{69}\text{Br}$	U	4.35
12	$^{26}\text{Si}(\alpha, p)^{29}\text{P}$	U	4.19
13	$^{26}\text{Si}(\alpha, p)^{29}\text{P}$	D	3.55
14	$^{72}\text{Kr}(p, \gamma)^{73}\text{Rb}$	D	2.85
15	$^{30}\text{S}(\alpha, p)^{33}\text{Cl}$	D	2.81
16	$^{56}\text{Ni}(p, \gamma)^{57}\text{Cu}$	U	1.89
17	$^{60}\text{Zn}(p, \gamma)^{61}\text{Ga}$	D	0.71
18	$^{72}\text{Kr}(p, \gamma)^{73}\text{Rb}$	U	0.29

^a Up(U) and down(D) represent the reaction rate changes of $\times 100$ and $/100$, respectively.

^b $E_{LC}^{(k)}$ in units of 10^{37} erg.

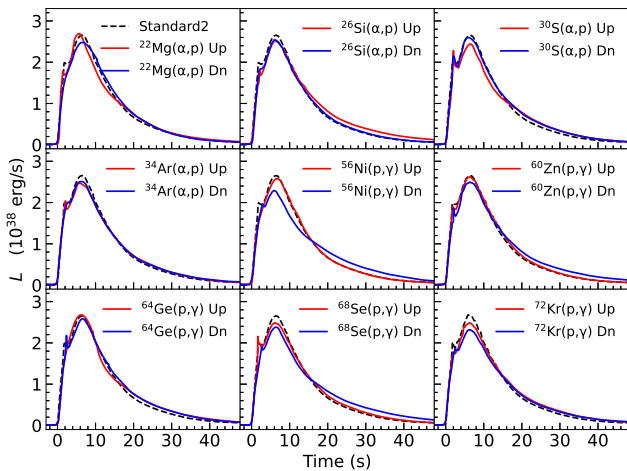
**Figure 9.** Same as Fig. 8 but the nuclear reactions are varied about the values used in standard model 2.

Fig. 8 shows the changes in double-peaked burst light curves induced by variation in (α, p) and (p, γ) reaction rates based on standard model 1. It is found that $^{68}\text{Se}(p, \gamma)^{69}\text{Br}$ -reaction with a factor by $\times 100$ will decrease the luminosity of the two peaks, it is the most sensitive reaction on the double-peaked bursts. The sequence of the sensitivity of the nuclear reaction waiting points can be found in Table 1.

Similarly, Fig. 9 shows the changes in double-peaked burst light curves induced by variation in (α, p) and (p, γ) reaction rates but the nuclear reactions are varied about the values used in standard model 2. We find that the double-peaked structure will disappear if the $^{56}\text{Ni}(p, \gamma)^{57}\text{Cu}$ -reaction and $^{64}\text{Ge}(p, \gamma)^{65}\text{As}$ -reaction were faster by a factor 100, the $^{22}\text{Mg}(\alpha, p)^{25}\text{Al}$ -reaction were slower by a factor 100. Table 2 summarizes the nuclear reaction waiting points that impact the double-peaked light curve in a sequence of sensitivity.

In this case, $^{68}\text{Se}(p, \gamma)^{69}\text{Br}$ -reaction with the reaction rate changes of $/100$ is the most sensitive reaction on the double-peaked bursts.

From the above analysis, we can find that the effect of the uncertainty in the theoretical reaction rates at waiting points is differed by the conditions of the double-peaked bursts. ^{22}Mg , ^{56}Ni , ^{64}Ge , ^{68}Se are possibly the most important nuclear waiting points impedance in the thermonuclear reaction flow to explain the double-peaked bursts.

4 DISCUSSION

So far, only a little attention has been paid to the model-observation comparisons and the final products of the double-peaked bursts, we will discuss these issues with the above calculations.

4.1 Model-observation comparisons

Li et al. (2021) analysed 16 multi-peaked type I X-ray bursts from 4U 1636-53 with the Rossi X-ray Timing Explorer (RXTE), where 14 double-peaked bursts were included. However, only one Obsid has been studied for its spectral evolution (as shown in Fig. 5 from (Li et al. 2021)). Chen et al. (2023) studied 10 thermonuclear bursts from 4U 1730-22 with Insight-HXMT during its two outbursts in 2021 & 2022, and found one double-peaked burst. We take the values of the first ($t_{p,1}$) and second ($t_{p,2}$) peak time, the first and second peak flux ratio ($r_{1,2}$) and the peak separation time (δt) from the spectral evolution of the bolometric flux about the above two observations, the values are illustrated in Table 3.

Fig. 10 shows the comparison between our models and the observations shown in Table 3, where our theoretical models are varied in mass accretion rate, metallicity, base heating, as well as the uncertainty of the nuclear reaction waiting points. We can see that the values of the first peak time $t_{p,1}$ are in the range of $\sim 1 - 4$ s, the second peak time $t_{p,2}$ is in the range of $\sim 6 - 8$ s, the peak separation time is in the range of $\sim 3 - 6$ s, and the peak flux ratio is in the range of $\sim 0.5 - 2.5$. The observational values of 4U 1636-53 with Obsid 60032-01-13-01 can be well explained with the changes in the parameters based on standard model 2. However, our nuclear origins models still can not explain the double-peaked burst with the longer peak separation time (e.g. 4U 1730-22 with $\delta t > 7$ s).

4.2 Final products during double-peaked bursts nucleosynthesis

We discuss the final products during the double-peaked type I X-ray burst nucleosynthesis. The compositional inertia due to the leftover of H, He, and CNO nuclei of the previous bursts can have important implications for the properties of subsequent burst (Taam 1980; Woosley et al. 2004). In Figs. 11 and 12, we show a succession of double-peaked bursts for standard models 1 and 2, we can see that the ashes of the previous burst affect the properties of the subsequent burst, which leads to the shape of the double-peaked bursts and final products are different from each burst in one model. Fig. 13 shows the averaged final products with standard models 1 and 2. Besides, we calculate the final products during the single-peaked bursts of nucleosynthesis for comparison. As we see, nuclei heavier than ^{56}Ni are poorly synthesized for double-peaked bursts, especially for standard model 1 with low mass accretion rate and metallicity. This is because the first peak of a double-peaked burst is caused by a pure helium burst, the amount of pure helium layer of standard model 1 is greater than that in standard model 2, and as a result, the leftover hydrogen of standard model 1 is less than that in standard model 2.

Table 3. Observational values of the peak ratio ($r_{1,2}$), the first ($t_{p,1}$) and second ($t_{p,2}$) peak time, and the peak separation time (δt) from 4U 1636-53 (Li et al. 2021) and 4U 1730-22 (Chen et al. 2023).

Source	mission	date	Obsid	$r_{1,2}$	$t_{p,1}$ (s)	$t_{p,2}$ (s)	δt (s)
4U 1636-53	RXTE	20011003	60032-01-13-01	0.73	3.10	7.10	4.00
4U 1730-22	Insight-HXMT	20220509	P051400201003-20220509-01-01	0.76	1.00	8.50	7.50

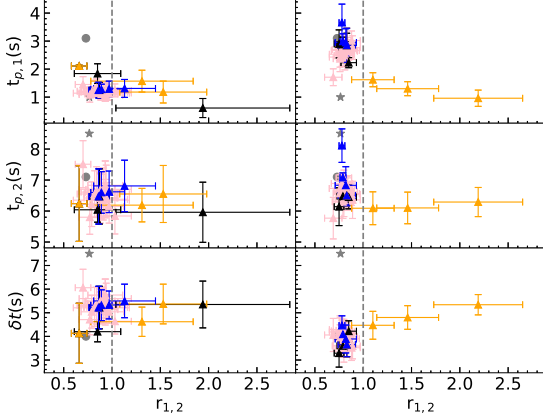


Figure 10. The first ($t_{p,1}$) and second ($t_{p,2}$) peak time, the peak separation time (δt) as a function of peak ratio ($r_{1,2}$). Black: the averaged values with 1σ errorbars under the variation in mass accretion rate. Orange: the averaged values with 1σ errorbars under the variation in metallicity. Blue: the averaged values with 1σ errorbars under the variation in base heating. Pink: the averaged values with 1σ errorbars under the variation in nuclear reaction waiting points. Solid circle: the values from the observations of 4U 1636-53. Star: the values from the observations of 4U 1730-22.

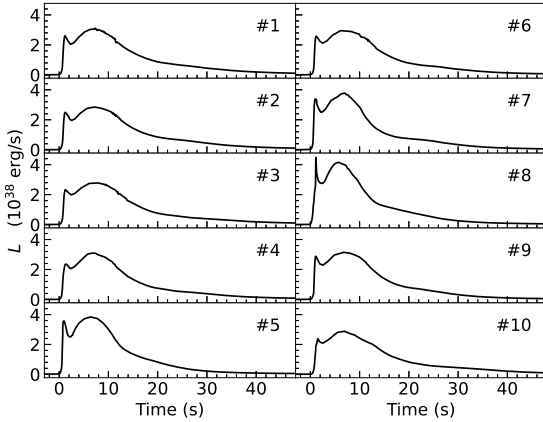


Figure 11. Samples of a succession of the double-peaked bursts for standard model 1 with $X = 0.7325$, $Y = 0.2575$, $Z = 0.01$, $\dot{M} = 5 \times 10^{-10} M_{\odot}/\text{yr}$, $Q_b = 0.1 \text{ MeV/u}$.

Finally, the heavier p-nuclei due to the rp process during the double-peaked bursts nucleosynthesis of standard model 1 is less than that in standard model 2.

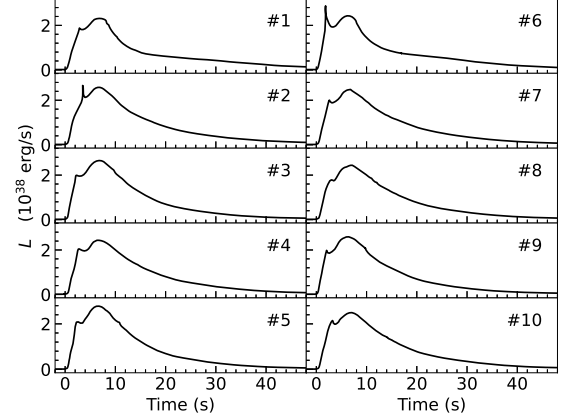


Figure 12. Same as Fig. 11 but for standard model 2 with $X = 0.6225$, $Y = 0.3275$, $Z = 0.05$, $\dot{M} = 5 \times 10^{-9} M_{\odot}/\text{yr}$, $Q_b = 0.1 \text{ MeV/u}$.

5 CONCLUSIONS

In this work, we investigate the nuclear origins of double-peaked bursts with low mass accretion rate at low metallicity (standard model 1) and one order of magnitude higher mass accretion rate at high metallicity (standard model 2) using MESA. We take into account the variation in mass accretion rate (models 3-10), metallicity (models 11-17), base heating (models 18-23), and nuclear reaction waiting points (Tables 1 and 2) to study the properties of the double-peaked bursts. Moreover, we make a comparison between our models and the observations from 4U 1636-53 and 4U 1730-22, the final products during double-peaked bursts nucleosynthesis are also explored. Our conclusions are as follows:

1. As the mass accretion rate increases, the dual-peak luminosity of double-peaked bursts decreases, the first peak time increases, the second peak time remains constant, and the peak separation time decreases. The double-peaked structure disappears at $\dot{M} = 9 \times 10^{-10} M_{\odot}/\text{yr}$ for $Z = 0.01$, at $\dot{M} = 9 \times 10^{-9} M_{\odot}/\text{yr}$ for $Z = 0.05$, which gives the parameter space for the double-peaked bursts, i.e., \dot{M} should be in the range of $\sim (4-8) \times 10^{-10} M_{\odot}/\text{yr}$ for $Z = 0.01$, in the range of $\sim (4-8) \times 10^{-9} M_{\odot}/\text{yr}$ for $Z = 0.05$.

2. As the metallicity increases, the peak luminosity of the first peak decreases, the second peak luminosity changes irregularly, the first peak time decreases, the second peak time remains constant, the peak separation time increases. The double-peaked structure disappears at $Z = 0.005$ for $\dot{M} = 8 \times 10^{-10} M_{\odot}/\text{yr}$, at $Z = 0.04$ for $\dot{M} = 5 \times 10^{-9} M_{\odot}/\text{yr}$.

3. As the base heating increases, the peak luminosity of the two peaks decreases, both the first and second peak times increase and the peak separation time increases. The double-peaked structure will not disappear with a change of Q_b in the range of $\sim 0.1 - 0.4 \text{ MeV/u}$.

4. The uncertainty in the nuclear reaction waiting points: ^{22}Mg , ^{26}Si , ^{30}S , ^{34}Ar , ^{56}Ni , ^{60}Zn , ^{64}Ge , ^{68}Se , ^{72}Kr has been explored. We

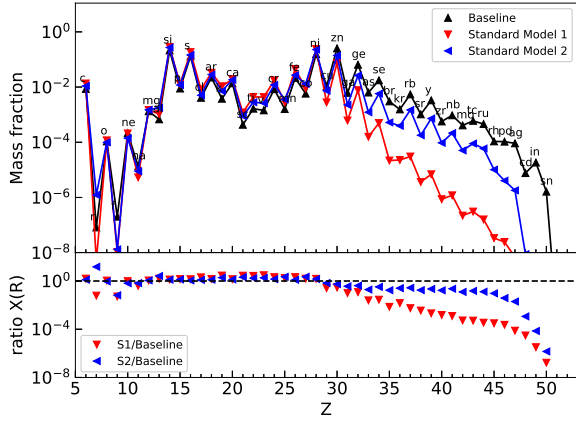


Figure 13. The averaged final products for each charge number at the burst tail end with different X-ray burst models. Red: double-peaked bursts from our standard model 1 (S1) with $M = 1.4M_{\odot}$, $R = 11.2$ km, $X = 0.7325$, $Y = 0.2575$, $Z = 0.01$, $Q_b = 0.1$ MeV/u, $\dot{M} = 5.0 \times 10^{-10} M_{\odot}/\text{yr}$. Blue: double-peaked bursts from our standard model 2 (S2) with $M = 1.4M_{\odot}$, $R = 11.2$ km, $X = 0.6225$, $Y = 0.3275$, $Z = 0.05$, $Q_b = 0.1$ MeV/u, $\dot{M} = 5.0 \times 10^{-9} M_{\odot}/\text{yr}$. Black: Single-peaked bursts with $M = 1.4M_{\odot}$, $R = 11.2$ km, $X = 0.70$, $Y = 0.28$, $Z = 0.02$, $Q_b = 0.1$ MeV/u, $\dot{M} = 1.9 \times 10^{-9} M_{\odot}/\text{yr}$, the model is named as baseline model. The lower panel displays the mass fraction ratio of the double-peaked bursts to single-peaked bursts.

find that ^{22}Mg , ^{56}Ni , ^{64}Ge , ^{68}Se are possibly the most important nuclear waiting points impedance in the thermonuclear reaction flow to explain the double-peaked bursts.

5. From the model-observation comparison, we find that our nuclear origins of double-peaked bursts can explain the observations such as 4U 1636-53, but it is difficult to explain the observations from 4U 1730-22, which has a large second peak time ($t_{p,2} \approx 8.5$ s) and peak separation time ($\delta t \approx 7.5$ s).

6. The final products during double-peaked bursts of nucleosynthesis are different from that during the single-peaked bursts of nucleosynthesis especially for nuclei heavier than ^{56}Ni . The heavier p-nuclei due to the rp process during the double-peaked bursts are less than that in single-peaked bursts.

These findings contribute to our comprehension of the diversity observations in double-peaked bursts. However, we can not give a comprehensive parameter space considering more models due to our computational limitation, it is worthwhile for scanning the whole grid of \dot{M} and z parameters to find other pairs of values that would produce double-peaked bursts. As the multi-peaked type I X-ray bursts are not observed with regularity, and the distance of the source is uncertain, we do not compare the light curves of the double-peaked bursts but the properties of the double-peaked bursts (e.g., $L_{p,1}$, $L_{p,2}$, $t_{p,1}$, $t_{p,2}$, δt). Besides, the values of burst strength (α), burst energy (E_{burst}), recurrence time (ΔT), the first ($L_{p,1}$) and second ($L_{p,2}$) peak luminosity are obtained from our models. However, these values from observations have rarely been studied. The comparisons of these values between the theory and observations are important for our understanding of the nuclear origins of double-peaked bursts, we leave this issue in our future work.

ACKNOWLEDGEMENTS

We appreciate the anonymous referee for helpful comments. We thank M. Hashimoto for his encouragement. We thank W. Wang and A. Dohi for the fruitful discussion. This work received the generous support of the National Natural Science Foundation of China Nos. 12263006, U2031204, 12163005, 12373038, and the Major Science and Technology Program of Xinjiang Uygur Autonomous Region under Grant No. 2022A03013-3.

DATA AVAILABILITY

The data underlying this article are available in this article.

REFERENCES

- Ayasli S., Joss P. C., 1982, *ApJ*, **256**, 637
 Bhattacharyya S., Strohmayer T. E., 2006, *ApJ*, **641**, L53
 Bult P., et al., 2019, *ApJ*, **885**, L1
 Bult P., et al., 2022, *ApJ*, **940**, 81
 Chen Y.-P., et al., 2023, *ApJ*, **942**, L12
 Cyburt R. H., et al., 2010, *ApJS*, **189**, 240
 Cyburt R. H., Amthor A. M., Heger A., Johnson E., Keek L., Meisel Z., Schatz H., Smith K., 2016, *ApJ*, **830**, 55
 Dohi A., Nishimura N., Hashimoto M., Matsuo Y., Noda T., Nagataki S., 2021, *ApJ*, **923**, 64
 Fisker J. L., Thielemann F.-K., Wiescher M., 2004, *ApJ*, **608**, L61
 Fisker J. L., Tan W., Görres J., Wiescher M., Cooper R. L., 2007, *ApJ*, **665**, 637
 Fujimoto M. Y., Hanawa T., Miyaji S., 1981, *ApJ*, **247**, 267
 Fujimoto M. Y., Sztajno M., Lewin W. H. G., van Paradijs J., 1988, *A&A*, **199**, L9
 Galloway D. K., Keek L., 2021, in Belloni T. M., Méndez M., Zhang C., eds, *Astrophysics and Space Science Library* Vol. 461, *Timing Neutron Stars: Pulsations, Oscillations and Explosions*. pp 209–262 ([arXiv:1712.06227](https://arxiv.org/abs/1712.06227)), doi:10.1007/978-3-662-62110-3_5
 Galloway D. K., Muno M. P., Hartman J. M., Psaltis D., Chakrabarty D., 2008, *ApJS*, **179**, 360
 Güver T., et al., 2021, *ApJ*, **910**, 37
 Haensel P., Zdunik J. L., 1990, *A&A*, **227**, 431
 Hanawa T., Fujimoto M. Y., 1984, *PASJ*, **36**, 199
 Heger A., Cumming A., Galloway D. K., Woosley S. E., 2007, *ApJ*, **671**, L141
 Hu J., et al., 2021, *Phys. Rev. Lett.*, **127**, 172701
 Jaiswal G. K., et al., 2019, *ApJ*, **883**, 61
 Johnston Z., Heger A., Galloway D. K., 2020, *MNRAS*, **494**, 4576
 Keek L., Cyburt R. H., Heger A., 2014, *ApJ*, **787**, 101
 Kuulkers E., Homan J., van der Klis M., Lewin W. H. G., Méndez M., 2002, *A&A*, **382**, 947
 Lampe N., Heger A., Galloway D. K., 2016, *ApJ*, **819**, 46
 Lewin W. H. G., van Paradijs J., Taam R. E., 1993, *Space Sci. Rev.*, **62**, 223
 Li C., Zhang G., Méndez M., Wang J., Lyu M., 2021, *MNRAS*, **501**, 168
 Liebendörfer M., Rosswog S., Thielemann F.-K., 2002, *ApJS*, **141**, 229
 Liu H., Gao Y., Li Z., Dohi A., Wang W., Lü G., Xu R., 2023, *MNRAS*, **525**, 2054
 Meisel Z., 2018, *ApJ*, **860**, 147
 Melia F., 1987, *ApJ*, **315**, L43
 Melia F., Zylstra G. J., 1992, *ApJ*, **398**, L53
 Paczynski B., 1983, *ApJ*, **267**, 315
 Paxton B., Bildsten L., Dotter A., Herwig F., Lesaffre P., Timmes F., 2011, *ApJS*, **192**, 3
 Paxton B., et al., 2013, *ApJS*, **208**, 4
 Paxton B., et al., 2015, *ApJS*, **220**, 15
 Paxton B., et al., 2018, *ApJS*, **234**, 34
 Penninx W., van Paradijs J., Lewin W. H. G., 1987, *ApJ*, **321**, L67

- Penninx W., Damen E., Tan J., Lewin W. H. G., van Paradijs J., 1989, *A&A*, [208](#), [146](#)
- Pike S. N., et al., 2021, *ApJ*, [918](#), [9](#)
- Rauscher T., Thielemann F.-K., 2000, *Atomic Data and Nuclear Data Tables*, [75](#), [1](#)
- Regev O., Livio M., 1984, *A&A*, [134](#), [123](#)
- Schatz H., Rehm K. E., 2006, *Nuclear Phys. A*, [777](#), [601](#)
- Strohmayer T., Bildsten L., 2006, in , Vol. 39, Compact stellar X-ray sources. pp 113–156
- Sztajno M., van Paradijs J., Lewin W. H. G., Trumper J., Stollman G., Pietsch W., van der Klis M., 1985, *ApJ*, [299](#), [487](#)
- Taam R. E., 1980, *ApJ*, [241](#), [358](#)
- Woosley S. E., et al., 2004, *ApJS*, [151](#), [75](#)
- Zhang G., Méndez M., Altamirano D., Belloni T. M., Homan J., 2009, *MNRAS*, [398](#), [368](#)
- Zhen G., et al., 2023, *ApJ*, [950](#), [110](#)

This paper has been typeset from a $\text{\TeX}/\text{\LaTeX}$ file prepared by the author.

Table 1. Physical inputs of the double-peaked bursts models and the burst number in each model, where N_T represents the total bursts number, N_D represents the double-peaked bursts number

Standard Model	X(H)	Y(He)	Z	Q_b (MeV/u)	\dot{M} ($10^{-9}M_\odot/\text{yr}$)	N_D/N_T
1	0.7325	0.2575	0.01	0.10	0.5	24/24
2	0.6225	0.3275	0.05	0.10	5	16/30
Model Number	X(H)	Y(He)	Z	Q_b (MeV/u)	\dot{M} ($10^{-9}M_\odot/\text{yr}$)	N_D/N_T
3	0.7325	0.2575	0.01	0.1	0.4	17/17
4	0.7325	0.2575	0.01	0.1	0.7	11/22
5	0.7325	0.2575	0.01	0.1	0.8	6/21
6	0.7325	0.2575	0.01	0.1	0.9	0/12
7	0.6225	0.3275	0.05	0.1	4	13/33
8	0.6225	0.3275	0.05	0.1	7	7/30
9	0.6225	0.3275	0.05	0.1	8	6/29
10	0.6225	0.3275	0.05	0.1	9	0/29
11	0.74625	0.24875	0.005	0.1	0.8	0/14
12	0.71875	0.26625	0.015	0.1	0.8	21/24
13	0.705	0.275	0.02	0.1	0.8	19/25
14	0.65	0.31	0.04	0.1	5	0/17
15	0.5675	0.3625	0.07	0.1	5	29/31
16	0.54	0.38	0.08	0.1	5	17/18
17	0.485	0.415	0.10	0.1	5	29/30
18	0.7325	0.2575	0.01	0.2	0.5	21/23
19	0.7325	0.2575	0.01	0.3	0.5	23/24
20	0.7325	0.2575	0.01	0.4	0.5	21/22
21	0.6225	0.3275	0.05	0.2	5	11/39
22	0.6225	0.3275	0.05	0.3	5	7/40
23	0.6225	0.3275	0.05	0.4	5	6/40

Table 2. The output quantities of the double-peaked burst models. The uncertainties of the output values indicate the 1σ standard deviation.

Standard Model	α	E_{burst} 10^{39} erg	$L_{p,1}$ 10^{38} erg/s	$L_{p,2}$ 10^{38} erg/s	ΔT h	$t_{p,1}$ s	$t_{p,2}$ s	δt s
1	74.95 ± 1.82	4.36 ± 0.56	2.91 ± 0.55	3.37 ± 0.59	15.46 ± 0.37	1.25 ± 0.28	6.47 ± 0.89	5.22 ± 0.90
2	67.32 ± 0.77	3.38 ± 0.24	2.06 ± 0.26	2.49 ± 0.14	1.08 ± 0.01	2.85 ± 0.43	6.50 ± 0.33	3.65 ± 0.51
Model Number	α	E_{burst} 10^{39} erg	$L_{p,1}$ 10^{38} erg/s	$L_{p,2}$ 10^{38} erg/s	ΔT h	$t_{p,1}$ s	$t_{p,2}$ s	δt s
3	96.46 ± 2.16	3.74 ± 0.95	5.85 ± 3.27	3.52 ± 1.04	18.79 ± 0.42	0.61 ± 0.34	5.96 ± 0.97	5.35 ± 0.99
4	73.01 ± 0.88	4.58 ± 0.28	2.33 ± 0.75	2.80 ± 0.52	11.57 ± 0.20	1.84 ± 0.35	6.04 ± 0.40	4.20 ± 0.43
5	72.07 ± 1.41	4.96 ± 0.46	1.81 ± 0.30	2.77 ± 0.58	10.28 ± 0.28	2.11 ± 0.03	6.24 ± 1.22	4.13 ± 1.27
6	71.85 ± 2.84	4.71 ± 0.36	-	2.38 ± 0.39	8.89 ± 0.36	-	6.99 ± 0.72	-
7	68.25 ± 0.69	3.28 ± 0.16	2.14 ± 0.25	2.51 ± 0.19	1.33 ± 0.01	2.23 ± 0.18	6.45 ± 0.38	4.22 ± 0.44
8	66.68 ± 1.12	3.53 ± 0.11	1.97 ± 0.16	2.45 ± 0.09	0.79 ± 0.01	2.88 ± 0.26	6.48 ± 0.23	3.60 ± 0.29
9	65.32 ± 0.88	3.56 ± 0.04	1.84 ± 0.15	2.44 ± 0.08	0.68 ± 0.01	2.90 ± 0.50	6.14 ± 0.61	3.29 ± 0.59
10	65.10 ± 1.31	3.59 ± 0.20	-	2.40 ± 0.19	0.62 ± 0.02	-	7.00 ± 0.23	-
11	70.57 ± 1.55	5.86 ± 0.80	-	2.21 ± 0.16	12.28 ± 0.26	-	6.83 ± 0.41	-
12	76.45 ± 1.11	3.96 ± 0.43	3.64 ± 1.47	2.79 ± 0.30	8.89 ± 0.13	1.57 ± 0.39	6.19 ± 0.54	4.62 ± 0.62
13	81.83 ± 1.88	3.31 ± 0.32	4.45 ± 1.42	2.93 ± 0.59	7.87 ± 0.18	1.18 ± 0.39	6.55 ± 0.92	5.37 ± 0.84
14	66.17 ± 1.08	3.79 ± 0.10	1.61 ± 0.24	2.35 ± 0.11	1.17 ± 0.02	3.12 ± 0.55	6.72 ± 0.44	3.60 ± 0.65
15	72.81 ± 1.45	2.81 ± 0.18	2.66 ± 0.35	2.46 ± 0.35	0.99 ± 0.02	1.62 ± 0.25	6.09 ± 0.53	4.47 ± 0.59
16	77.96 ± 1.39	2.54 ± 0.21	3.22 ± 0.52	2.26 ± 0.31	0.95 ± 0.02	1.30 ± 0.25	6.10 ± 0.51	4.80 ± 0.50
17	98.75 ± 1.33	1.91 ± 0.22	4.83 ± 0.83	2.24 ± 0.30	0.90 ± 0.02	0.96 ± 0.29	6.29 ± 0.41	5.34 ± 0.43
18	74.32 ± 1.35	4.34 ± 0.28	2.93 ± 0.56	3.31 ± 0.60	15.44 ± 0.27	1.28 ± 0.18	6.60 ± 0.67	5.32 ± 0.65
19	74.27 ± 0.81	4.26 ± 0.35	2.96 ± 0.69	3.06 ± 0.59	15.06 ± 0.20	1.29 ± 0.28	6.62 ± 0.67	5.33 ± 0.59
20	73.39 ± 0.70	4.04 ± 0.34	3.21 ± 1.46	2.79 ± 0.67	14.82 ± 0.23	1.31 ± 0.32	6.81 ± 0.83	5.50 ± 0.71
21	67.23 ± 1.03	3.30 ± 0.10	1.86 ± 0.16	2.27 ± 0.18	1.03 ± 0.03	2.95 ± 0.49	6.83 ± 0.60	3.89 ± 0.59
22	65.50 ± 0.45	3.28 ± 0.10	1.65 ± 0.13	2.11 ± 0.14	0.98 ± 0.02	2.99 ± 0.27	7.08 ± 0.15	4.09 ± 0.18
23	62.59 ± 1.27	2.96 ± 0.17	1.40 ± 0.11	1.77 ± 0.07	0.92 ± 0.01	3.66 ± 0.66	8.11 ± 0.54	4.46 ± 0.41